

High Conversion Efficiency Carbon Nanotube-Based Barrier-Free Bipolar-Diode Photodetector

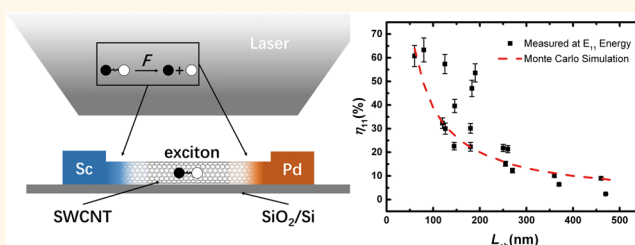
Fanglin Wang,[†] Sheng Wang,[†] Fengrui Yao,[§] Haitao Xu,[†] Nan Wei,[†] Kaihui Liu,^{§,||} and Lian-Mao Peng^{*,†}

[†]Key Laboratory for the Physics and Chemistry of Nanodevices, Department of Electronics, [§]State Key Laboratory for Mesoscopic Physics, School of Physics, and ^{||}Collaborative Innovation Center of Quantum Matter and Center for Nanochemistry, Peking University, Beijing 100871, China

Supporting Information

ABSTRACT: Conversion efficiency (CE) is the most important figure of merit for photodetectors. For carbon nanotubes (CNT) based photodetectors, the CE is mainly determined by excitons dissociation and transport of free carriers toward contacts. While phonon-assisted exciton dissociation mechanism is effective in split-gate CNT p–n diodes, the CE is typically low in these devices, approximately 1–5%. Here, we evaluate the performance of a barrier-free bipolar diode (BFBD), which is basically a semiconducting CNT asymmetrically contacted by perfect n-type ohmic contact (Sc) and p-type ohmic contact (Pd) at the two ends of the diode. We show that the CE in short channel BFBD devices (e.g., 60 nm) is over 60%, and it reduces rapidly with increasing channel length. We find that the electric-field-assisted mechanism dominates the dissociation rate of excitons in BFBD devices at zero bias and thus the photocurrent generation process. By performing a time-resolved and spatial-resolved Monte Carlo simulation, we find that there exists an effective electron (hole)-rich region near the n-type (p-type) electrode in the asymmetrically contacted BFBD device, where the electric-field strength is larger than 17 V/ μm and exciton dissociation is extremely fast (<0.1 ps), leading to very high CE in the BFBD devices.

KEYWORDS: carbon nanotube, CNT diode, BFBD, IR detector, exciton dissociation



Semiconducting single-walled carbon nanotube (s-SWCNT) is the subject of extensive study in both nanoelectronics and nanophotonics as a possible replacement of silicon-based transistors and photodetectors.^{1,2} For photodetectors, conversion efficiency (η) is the most essential figure of merit. Due to the quasi one-dimensional nature of the SWCNT, photoexcited excitons with binding energy of hundreds of meV dominate the photocurrent spectra of carbon nanotube (CNT)-based detectors.^{3–5} However, the mechanism as to how excitons, which cannot contribute directly to photocurrent, are dissociated into free carriers is still under discussion.

Recently, phonon-assisted dissociation mechanism was confirmed as one possible channel in split-gate p–n diodes.⁶ Compared to traditional detectors, the conversion efficiency (1–5%) of these diodes is low, which is ultimately limited by the low phonon density involved.^{6,7} Another possible mechanism is electric-field-induced dissociation,⁸ which might exist in barrier-free bipolar diodes (BFBDs).⁹ In these devices, phonon-assisted exciton dissociation is negligible. This is because the exciton binding energy in a CNT is typically higher than the optical phonon energy (0.18–0.2 eV), and phonon energy dissipation to the substrate in BFBDs is

prominent.^{10–14} However, how excitons in these devices dissociate and whether the efficiency is better or not than that of split-gate p–n diodes have never been studied.

RESULTS AND DISCUSSION

In this paper, we first evaluate quantitatively the conversion efficiency of BFBDs by measuring photocurrent spectra under the first (E_{11}) and second (E_{22}) exciton resonance excitations. Figure 1a shows a representative false-colored scanning electron microscopy (SEM) image and a schematic diagram of a BFBD. The CNTs used in this study are grown on an n⁺ silicon/SiO₂ substrate using chemical vapor deposition (CVD) method. Palladium (Pd) and scandium (Sc) electrodes are deposited by the standard e-beam exposure and deposition methods. All results discussed in this paper are obtained from 19 BFBD devices fabricated on the same s-SWCNT. These BFBDs exhibit excellent rectification behavior. Current and voltage (I – V) curves of three BFBD devices with different

Received: July 28, 2016

Accepted: September 15, 2016

Published: September 15, 2016

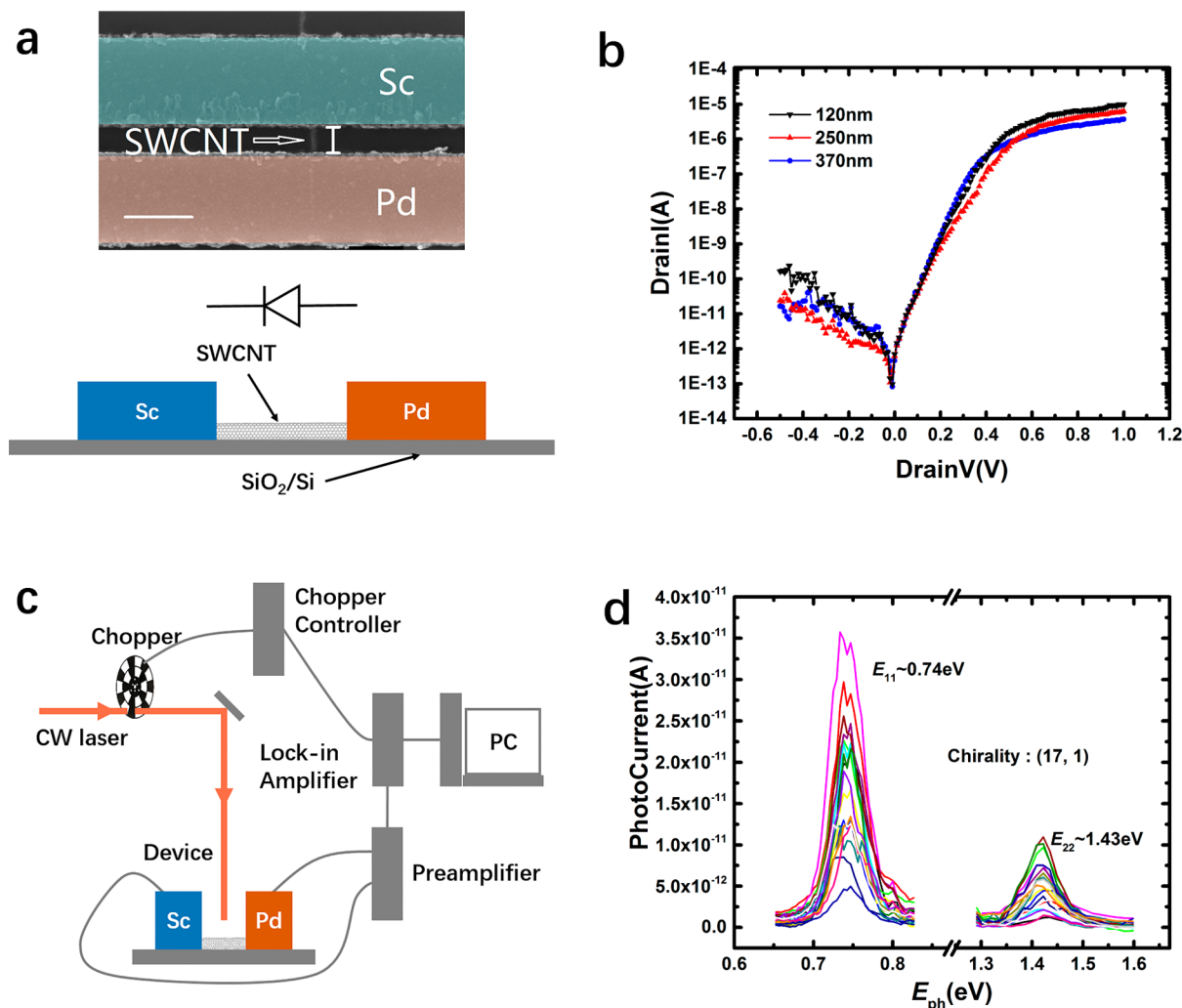


Figure 1. Geometry and performance of BFBDs using asymmetric p-type (Pd) and n-type (Sc) contacts. (a) A representative false-colored SEM image and a schematic diagram of a BFBD. (b) I - V curves of three BFBD devices fabricated on the same (17, 1) SWCNT but with different channel lengths. (c) Experimental setup for measuring photocurrent spectra. The device is working at zero-bias and zero-gate-voltage condition. (d) Photocurrent spectra of totally 19 BFBD devices fabricated on the same (17, 1) SWCNT but with different channel lengths.

channel lengths are shown in Figure 1b. We now consider evaluating the photocurrent conversion efficiencies (η) under the E_{11} and E_{22} exciton resonance conditions. The η for the i th ($i = 1, 2$) resonance is defined as

$$\eta_{ii} = \frac{I_{ii}(E)}{qN\Phi(E) \cdot \sigma_{ii}} \quad (1)$$

where $I_{ii}(E)$ is the photocurrent under the i th exciton resonance, q is the elementary charge, and Φ is the photon flux (measured in photon per unit time and per area). $N = L_{\text{ch}} \cdot 4(n^2 + nm + m^2)^{1/2} / \alpha\sqrt{3}$ is the number of carbon atoms within the channel, where n and m are the chirality numbers of the tube, $\alpha = 0.249$ nm is the lattice constant for carbon nanotubes, L_{ch} is the channel length, and σ_{ii} is the absorption cross section per carbon atom.

To measure the photocurrent in BFBD devices, a lock-in technique is employed. The experimental setup is depicted in Figure 1c. Figure 1d shows the photocurrent spectra obtained from 19 BFBD devices with different channel lengths around E_{11} and E_{22} photoexcitation. All BFBD devices were fabricated on the same SWCNT, and its chirality is determined to be (17, 1) by minimizing the residual energy, $E_{\text{res}}^2 = \sum_i (E_{ii, \text{Atlas}}^k -$

$E_{ii, \text{PC}})^2$, where $E_{ii, \text{PC}}$ is the i th peak energy in photocurrent spectra and $E_{ii, \text{Atlas}}^k$ is the reference resonance energy,¹⁵ respectively. E_{res} is the distance in energy space between the measured exciton resonances and the nearest match in the CNT Atlas. The minimized E_{res} is approximately 30 meV, which is in the same range of experimental uncertainty reported in optical absorption experiments and photocurrent resonances experiments.^{16,17}

To calculate the conversion efficiency, we employed an empirical relation of the spectral weight. Spectral weight is defined as the integration of the absorption cross section with respect to photo energy, which can be written as $S_{ii} \equiv \int \sigma_{ii} dE$, where i ($= 1, 2$) represents the i th transition. It is shown, both theoretically and experimentally, that the dependence of the spectral weight on nanotube diameter can be captured by the relations:¹⁸ $S_{11} \approx 0.8/d_t$ and $S_{22} \approx 0.73/d_t^{0.68}$, where d_t is the tube diameter in unit of nm and S_{ii} is in unit of 10^{-17} cm²eV. The conversion efficiency is thus given by

$$\eta_{ii} = \frac{\int \eta_{ii} \sigma_{ii} dE}{S_{ii}} \quad (2)$$

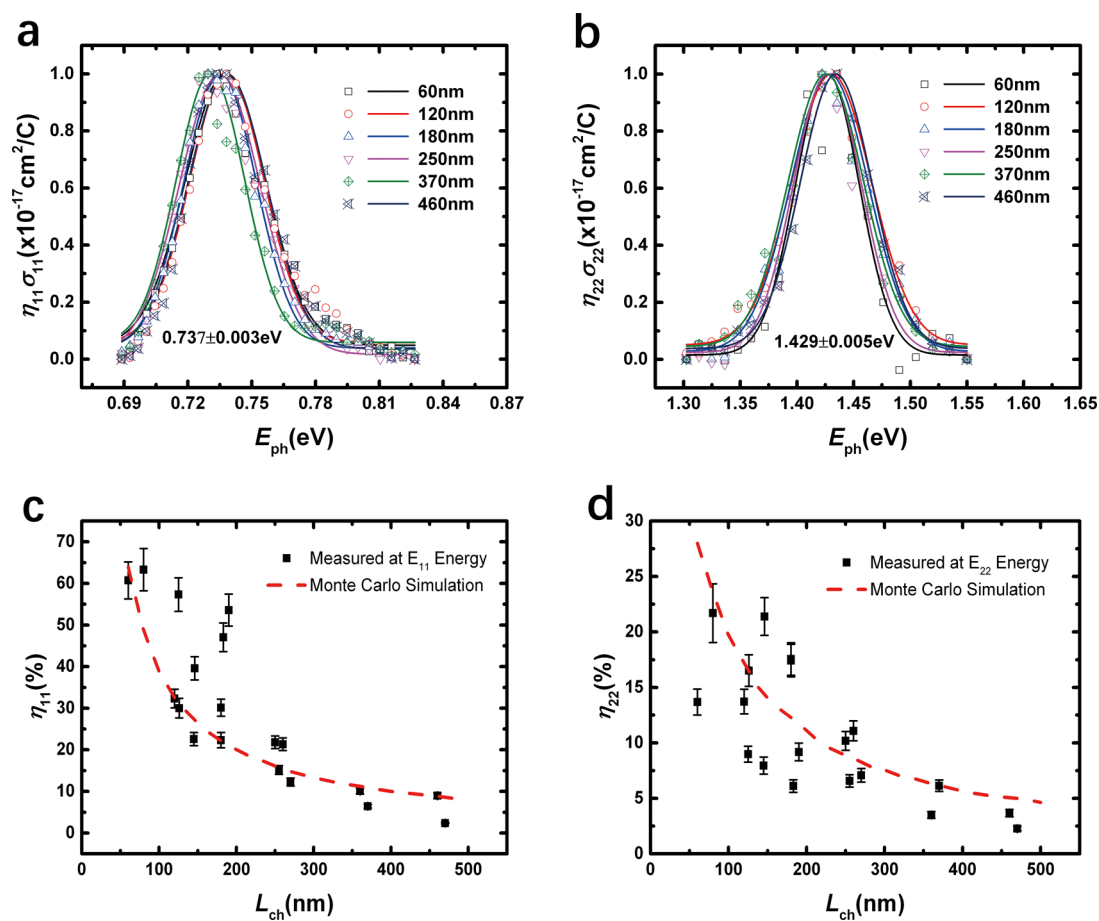


Figure 2. Experimental raw data and extracted conversion efficiencies. (a–b) Experimental and normalized fitting curves of $\eta_{11}\sigma_{11}$ and $\eta_{22}\sigma_{22}$ for devices fabricated on the same (17, 1) SWCNT but with different channel lengths. Discrete symbols represent experimental data, and solid lines are Lorentzian fit of these data. (c and d) Conversion efficiencies η_{11} (c) and η_{22} (d) for BFBF devices with different channel lengths under the E_{11} and E_{22} photoexcitation, respectively. The red dash lines in (c) and (d) are simulated conversion efficiency for devices with different channel lengths using Monte Carlo method. The best fit between experimental and simulation results is obtained for $L_{\text{eff}} \sim 12$ nm.

Table 1. Data Related to the First Exciton Peaks

dev.	L_{ch} (nm)	E_{11} (eV)	fwhm $_{11}$ (eV)	$\sigma_{11}\eta_{11} \times 10^{-17}$ cm 2	$S_{11}\eta_{11} \times 10^{-20}$ cm 2 eV	η_{11}	$\sigma_{11} \times 10^{-17}$ cm 2 /C
1	60	0.738	0.045	4.520	0.179	0.607	7.4
2	80	0.741	0.041	5.456	0.187	0.633	8.6
3	120	0.738	0.041	2.918	0.095	0.324	9.0
4	125	0.739	0.044	4.837	0.169	0.573	8.4
5	126	0.74	0.039	2.903	0.089	0.300	9.7
6	145	0.739	0.044	1.881	0.067	0.226	8.3
7	146	0.741	0.044	3.319	0.117	0.396	8.4
8	180	0.742	0.040	2.056	0.066	0.223	9.2
9	180	0.735	0.040	2.740	0.089	0.301	9.1
10	183	0.737	0.042	3.987	0.139	0.470	8.5
11	190	0.735	0.045	4.370	0.158	0.536	8.2
12	250	0.735	0.045	1.737	0.064	0.218	8.0
13	255	0.731	0.044	1.236	0.045	0.151	8.2
14	260	0.737	0.039	2.058	0.063	0.213	9.6
15	270	0.735	0.049	0.867	0.036	0.123	7.1
16	360	0.736	0.044	0.800	0.030	0.101	7.9
17	370	0.731	0.038	0.634	0.019	0.064	9.8
18	460	0.738	0.043	0.753	0.026	0.090	8.4
19	470	0.739	0.045	0.194	0.007	0.024	8.1
average		0.737	0.043				8.5
variance		0.003	0.003				0.7

Table 2. Data Related to the Second Exciton Peaks

dev.	L_{ch} (nm)	E_{22} (eV)	fwhm_{22} (eV)	$\sigma_{22}\eta_{22} \times 10^{-17}$ cm ²	$S_{22}\eta_{22} \times 10^{-20}$ cm ² eV	η_{22}	$\sigma_{22} \times 10^{-17}$ cm ² /C
1	60	1.427	0.066	0.593	0.041	0.137	4.3
2	80	1.433	0.073	0.878	0.065	0.217	4.0
3	120	1.431	0.083	0.492	0.041	0.137	3.6
4	125	1.437	0.080	0.319	0.027	0.090	3.6
5	126	1.431	0.084	0.594	0.050	0.165	3.6
6	145	1.434	0.085	0.311	0.024	0.079	3.9
7	146	1.426	0.073	0.867	0.064	0.214	4.1
8	180	1.436	0.077	0.668	0.053	0.176	3.8
9	180	1.429	0.080	0.627	0.052	0.174	3.6
10	183	1.429	0.081	0.243	0.018	0.061	4.0
11	190	1.423	0.074	0.036	0.028	0.092	3.9
12	250	1.428	0.071	0.417	0.031	0.102	4.1
13	255	1.429	0.073	0.267	0.020	0.066	4.1
14	260	1.422	0.073	0.449	0.033	0.111	4.1
15	270	1.425	0.069	0.304	0.021	0.071	4.3
16	360	1.439	0.073	0.136	0.011	0.035	3.9
17	370	1.425	0.078	0.231	0.018	0.061	3.8
18	460	1.434	0.074	0.144	0.011	0.037	3.9
19	470	1.42	0.071	0.094	0.007	0.023	4.1
average		1.429	0.076				3.9
variance		0.005	0.005				0.2

We note that although η_{ii} is energy dependent, which changes a little over the energy range around the i th exciton resonances (about tens of meV) and is thus assumed to be a constant in the integration in eq 2.¹⁸ The product of the cross section per atom with the conversion efficiency can be derived by normalizing the photocurrent spectrum (e.g., Figure 1d), which is $\eta_{ii}\sigma_{ii} = I_{ii}(E)/qN\Phi(E)$. Fitting the $\eta_{ii}\sigma_{ii}$ curves for each exciton resonance to a Lorentzian profile, we derived the full width half-maximums (fwhms), peak positions, peak values, and integrated peak areas under each resonance. Figure 2a,b is the normalized $\eta_{ii}\sigma_{ii}$ and fitting curves for E_{11} and E_{22} resonances, respectively. Statistical analysis on results obtained from totally 19 devices with different channel lengths gives $\text{fwhm}_{11} = 43 \pm 3$ meV and $\text{fwhm}_{22} = 76 \pm 5$ meV; $E_{11} = 0.737 \pm 0.003$ eV and $E_{22} = 1.429 \pm 0.005$ eV for E_{11} and E_{22} exciton resonances, respectively. The peak area is the integration in eq 2. The conversion efficiency η_{ii} is obtained by dividing the peak area by the spectral weight S_{ii} . Moreover, σ_{ii} is derived by dividing the peak value of $\eta_{ii}\sigma_{ii}$ by the corresponding η_{ii} , yielding $\sigma_{11} = 8.5(\pm 0.7) \times 10^{-17}$ cm²/C and $\sigma_{22} = 3.9(\pm 0.2) \times 10^{-17}$ cm²/C, which are consistent with the previous reports on optical absorption experiments and photocurrent resonances experiments.^{15,18} These results are summarized in Tables 1 and 2.

Figure 2c,d shows the η_{11} and η_{22} obtained from 19 devices with different channel lengths, respectively. In long-channel BFBD devices, both η_{11} and η_{22} are in the same range as that found in split-gate diodes.¹⁸ However, these values increase in short channel-length devices. Under the E_{11} exciton resonance and at zero bias, the photocurrent in BFBDs results mainly from the dissociation of E_{11} excitons. Under the E_{22} exciton resonance, the photocurrent can be generated from the E_{11} continuum band before decaying into E_{11} excitons, but high bias voltage should be applied to extract carriers.^{19,20} Since BFBD works at zero-bias condition, η_{22} results also from the dissociation of E_{11} excitons. Two mechanisms have been proposed to explain exciton dissociation in CNTs, i.e., phonon-assisted dissociation and electric-field-assisted dissociation.^{6,8}

The prerequisites for the former mechanism are (1) exciton binding energy (E_b) is not larger than the optical phonon energy ($E_q = 0.18\text{--}0.2$ eV); and (2) optical phonon occupation number is high. However, E_b of (17, 1) nanotube is $E_q \sim 0.24$ eV, which is much larger than the optical phonon energy E_q .²¹ In addition, optical phonons in BFBDs can efficiently decay into the heat bath provided by the substrate, because the nanotube used in this work is not suspended.^{10,11,22,23} The phonon occupation number is thus very small, and the phonon-assisted dissociation mechanism is not the dominate mechanism for the BFBD device discussed here.

In principle, excitons can also be dissociated *via* electric-field-assisted dissociation mechanism, but this mechanism requires a high electric field. Applying a strong electric field along the tube axis, a bound exciton can dissociate into a free electron and a hole in the first continuum band. The dissociation rate is given by⁸

$$k_F(F) = \alpha \frac{E_b F_0}{\hbar F} \exp\left(-\frac{F_0}{F}\right) \quad (3)$$

where $F_0 = \beta E_b^{3/2} m^{1/2} / e\hbar$, m is a reduced exciton mass, F is the applied electric field, \hbar is the Planck constant, and $\alpha = 4.1$ and $\beta = 1.74$ are constants. The exciton binding energy $E_b \sim 0.34/d_t$,²¹ where d_t is the nanotube diameter and is in unit of nm. Given an electric field, we can calculate the exciton dissociation rate of the (17, 1) nanotube, which is plotted in Figure 3a. The rate is highly sensitive to the electric-field strength. When F is larger than 17 V/ μm , $k_F^{-1} < 0.1$ ps, and this time is more than 100 times shorter than the nonradiative lifetime of excitons in the nanotube (~ 10 ps).²⁴ Given this field, it is reasonable to assume that almost all excitons are dissociated by the field. On the other hand, k_F^{-1} increases rapidly with reducing F . When F is reduced to be < 13 V/ μm , the exciton lifetime then becomes comparable to the nonradiative lifetime of excitons. In this situation, electric-field-assisted exciton dissociation becomes less important and contributes little to the photocurrent.

The electric-field strength in a device is related to the charge distribution in the channel. In a BFBD, Pd (Sc) contact to the

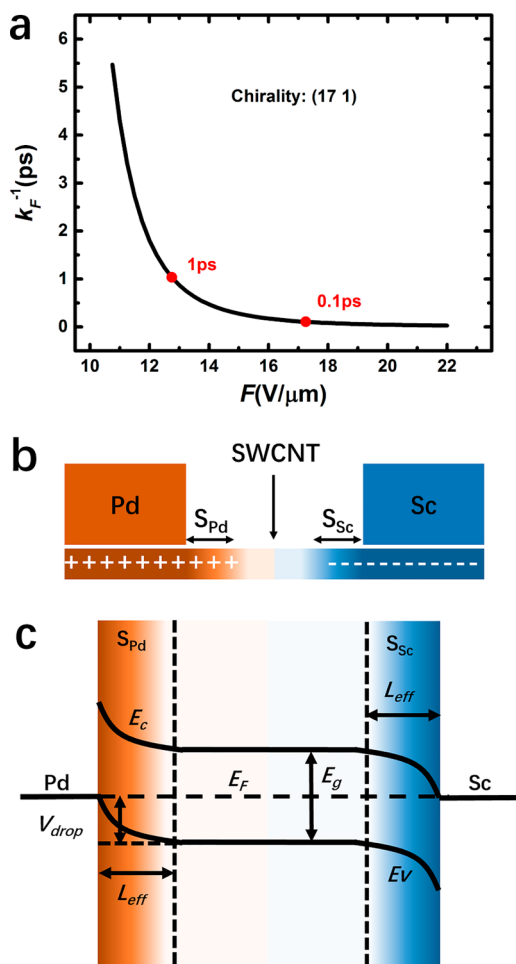


Figure 3. Exciton lifetime and schematic diagrams of charge transfer and electric field in a BFBD device. (a) Exciton lifetime (k_F^{-1}) in the (17, 1) nanotube as a function of electric field. Schematic diagrams illustrating (b) charge transfer between the CNT channel and n-type (Sc) and p-type (Pd) contacts; and (c) band bending near the contacts. Holes (electrons) transfer from the Pd (Sc) contact into the channel and decay within S_{Pd} (S_{Sc}), and the region between these two hole- and electron-rich regions is neutral with negligible amount of charge.

nanotube is in side-contact geometry, providing perfect ohmic contact to the valence (conduction) band of the s-SWCNT.^{13,25,26} Beneath the contact, there exists a small gap of around 0.3 nm between the metal and the nanotube because of van der Waals interactions.²⁷ At the interface, charges are transferred across the separation from the metal to the nanotube and are balanced by the image charges in the metal, of equal magnitude but opposite charge.^{28,29} The density of the transferred charges decays away from the interface into the channel.^{29,32} When both Pd and Sc are deposited on a s-SWCNT, the electrostatic attraction between holes from the Pd contact and electrons from the Sc contact will increase the density of both charges near the contact. Since the s-SWCNT used here is unintentionally doped, all charges in the CNT channel are injected or transferred from the contacts. Figure 3b shows a schematic diagram illustrating the net charge distribution in a BFBD.

In principle, electric field in a channel may be measured *via* atom force microscopy (AFM).^{30,31} Since the electric field drops quickly near the contact (S_{Pd} and S_{Sc} in Figure 3c), the

tip radius of the AFM should be very small to see the field variation near the contact. So far, no such experiment results have been reported. Here, we aim to estimate the electric-field strength to assess whether or not the build-in field in a BFBD is strong enough to dissociate excitons in device. In general, the contact barrier for holes can be written as²⁸

$$\Delta = \Delta_0 - eV_{CNT} \quad (4)$$

where V_{CNT} is the self-consistent electrostatic potential on the CNT channel with transferred charges, and $\Delta_0 = E_g + \chi - \Phi_m$, where E_g is the bandgap, χ is the electron affinity, and Φ_m is the metal work function. For the (17, 1) tube with a diameter $d_t = 1.39$ nm, the barrier is estimated to be $\Delta < 0.01$ eV.²⁸ For electrons, the contact barrier is similar, both electrons and holes can be injected without barriers into the s-SWCNT channel at room temperature when suitably biased. Figure 3c shows the band diagram of a BFBD. The voltage drop for holes from the Pd contact to the middle of the channel is $V_{drop} \sim -\Delta_0 \sim 0.5$ V. It is shown that the shortest channel length that can retain the rectifier characteristic in a BFBD is around 50 nm.³² Supposing a neutral region in the BFBD is ~ 10 nm, the region where the voltage V_{drop} takes place is then approximately 20 nm. If we assume a constant charge density within this region, the average field strength is 25 V/ μm , which is sufficiently large to induce excitons dissociation and to contribute to the photocurrent. The maximum electric-field strength in a real BFBD should be larger than this value, since realistic charge density drops much faster than the assumed linear form.²⁹ We conclude that excitons in (17, 1) will be effectively dissociated in this build-in electric filed.

Since exciton dissociation rate depends sensitively on the electric field (Figure 3a), to a first order approximation, we assume that there exists two effective regions (S_{Pd} and S_{Sc} in Figure 3b,c) near the Pd and Sc contact, where electric field is strong (e.g., >17 V/ μm) so that excitons can be effectively dissociated in these regions. Further into the nanotube channel, electric field is rapidly reduced, and electric-field-assisted dissociation is ignored. To estimate the width (L_{eff}) of these high field regions, we assume that S_{Pd} and S_{Sc} are of the same width, and we employ a time-resolved and spatial-resolved Monte Carlo simulation to model the excitons' dynamic behaviors in BFBD devices. We integrate the excitons dissociation over time and space to obtain the conversion efficiency (η):^{33–35}

$$\eta_{ii} = \frac{\iint k_F(x)n_{11}(x,t)dxdt}{\iint G_i(x,t)dxdt} \quad (5)$$

where G_i is the generating function of the excitation pulse for the E_{ii} photoexcitation and $i = 1, 2$. Details on the simulation are given in the Supporting Information. The width (L_{eff}) of S_{Pd} and S_{Sc} is found to be approximately 12 nm, which best describes the data presented in Figure 2c,d for conversion efficiencies of devices with different channel-lengths.

Careful examination of Figure 2c,d reveals that η_{11} is slightly larger than $2L_{eff}/L_{ch}$. This suggests that only a few excitons initially generated outside the high field regions (S_{Pd} and S_{Sc}) may diffuse into the these regions and contribute to photocurrent before disappearing *via* such effective processes as exciton–exciton annihilation and recombination in the low-field region.^{35–37} For E_{22} excitons, the decay rate (k_{21}^{-1}) from E_{22} state to E_{11} state is estimated to be $k_{21}^{-1} \sim 0.5$ ps. This value is consistent with results measured in femtosecond transient

absorption spectroscopic studies.^{34–36,38} This is the reason why η_{22} is generally lower than η_{11} in the same device because of the nonradiatively decay of E_{22} excitons by Auger recombination in the effective region.³⁹

CONCLUSIONS

In summary, we have shown that electric-field-assisted exciton dissociation mechanism dominates the photocurrent generation in BFBD devices. The exciton dynamics in the CNT is simulated by a time-resolved and spatial-resolved Monte Carlo model. We found that, effectively, there exists two high-field regions (~ 12 nm) near the n-type contact (Sc) and p-type contact (Pd), where as a result of charge transfer from the contacts, the field is larger than 17 V/ μm so that excited excitons within these regions may be effectively dissociated within 0.1 ps and contribute to photocurrent. This mechanism enables a high conversion efficiency of over 60% in short channel devices (e.g., 60 nm), but reduces rapidly in long channel devices where most of the low electric-field region contributes little to the photocurrent generation. So far, the CNT-based BFBD has been shown to be a promising candidate for applications in nanophotonics for its outstanding properties: high voltage output,⁴⁰ high dynamic range,⁴¹ small size,³² zero source–drain bias, ease of fabrication,⁹ and most importantly high conversion efficiency.

METHODS

Experimental Details. The light source used in this work is a super continuum wave (CW) laser (NKT photonics) which is assembled to a Raman system (Horiba Jobin-Yvon, HR800). The lock-in system consists of a lock-in amplifier (SRS, SR830), a chopper (SRS, SR540), and a current preamplifier (DL Instruments, Model 1211). A Labview program is designed to control the output laser wavelength and acquire signals simultaneously. To calculate the photon flux in the channel, the laser power is first measured using a Germanium photodetector (Thorlab, S122C). The Gaussian diameter (the diameter of the beam at which its intensity equals $1/e^2$ that of the maximum) of the laser spot is derived through cutting-edge measurement (Figure S3a). Considering the chromatic aberrations of the optical lens, we measured the Gaussian diameters every 50 nm in the range of laser wavelengths in photocurrent measurements, and interpolation method is employed to obtain $\phi(E)$ for E in the 50 nm gaps. The results obtained from measurements at the center of the first (E_{11}) and second (E_{22}) exciton resonances are shown in Figure S3b.

ASSOCIATED CONTENT

Supporting Information

The Supporting Information is available free of charge on the ACS Publications website at DOI: 10.1021/acs.nano.6b05047.

Details on the Monte Carlo simulation on the excitons dynamic behaviors in the channel, a schematic diagram illustrating the energy levels involved for exciton dissociation, and exciton populations for E_{11} and E_{22} states and a (17, 1) tube (PDF)

AUTHOR INFORMATION

Corresponding Author

*E-mail: impeng@pku.edu.cn.

Notes

The authors declare no competing financial interest.

ACKNOWLEDGMENTS

This work was supported by the Ministry of Science and Technology of China (grant no. 2016YFA0201902), National Science Foundation of China (grant nos. 61321001, 61427901-002, 61390504, and 61271051), and Beijing Municipal Science and Technology Commission (grant no. Z151100003315009).

REFERENCES

- (1) Avouris, Ph.; Freitag, M.; Perebeinos, V. Carbon-Nanotube Photonics and Optoelectronics. *Nat. Photonics* **2008**, *2*, 341–350.
- (2) Avouris, Ph.; Chen, Z. H.; Perebeinos, V. Carbon-Based Electronics. *Nat. Nanotechnol.* **2007**, *2*, 605–615.
- (3) Wang, F.; Dukovic, G.; Brus, L.; Heinz, T. The Optical Resonances in Carbon Nanotubes Arise from Excitons. *Science* **2005**, *308*, 838–841.
- (4) Spataru, C.; Ismail-Beigi, S.; Benedict, L.; Louie, S. Excitonic Effects and Optical Spectra of Single-Walled Carbon Nanotubes. *Phys. Rev. Lett.* **2004**, *92*, 077402.
- (5) Perebeinos, V.; Tersoff, J.; Avouris, Ph. Scaling of Excitons in Carbon Nanotubes. *Phys. Rev. Lett.* **2004**, *92*, 257402.
- (6) Chang, S. W.; Hazra, J.; Amer, M.; Kapadia, R.; Cronin, S. A Comparison of Photocurrent Mechanisms in Quasi-Metallic and Semiconducting Carbon Nanotube pn-Junctions. *ACS Nano* **2015**, *9*, 11551–11556.
- (7) Saleh, E. A. B.; Teich, C. M. *Fundamentals of Photonics*; John Wiley and Sons, Inc.: Hoboken, NJ, 1990; pp 645–661.
- (8) Perebeinos, V.; Avouris, Ph. Exciton Ionization, Franz-Keldysh, and Stark Effects in Carbon Nanotubes. *Nano Lett.* **2007**, *7*, 609–613.
- (9) Wang, S.; Zhang, L. H.; Zhang, Z. Y.; Ding, L.; Zeng, Q. S.; Wang, Z. X.; Liang, X. L.; Gao, M.; Shen, J.; Xu, H. L.; Chen, Q.; Cui, R. L.; Li, Y.; Peng, L. M. Photovoltaic Effects in Asymmetrically Contacted CNT Barrier-Free Bipolar Diode. *J. Phys. Chem. C* **2009**, *113*, 6891–6893.
- (10) Steiner, M.; Freitag, M.; Perebeinos, V.; Tsang, J. C.; Small, J. P.; Kinoshita, M.; Yuan, D. N.; Liu, J.; Avouris, P. Phonon Populations and Electrical Power Dissipation in Carbon Nanotube Transistors. *Nat. Nanotechnol.* **2009**, *4*, 320–324.
- (11) Perebeinos, V.; Avouris, Ph. Phonon and Electronic Non-radiative Decay Mechanisms of Excitons in Carbon Nanotubes. *Phys. Rev. Lett.* **2008**, *101*, 057401.
- (12) Yao, Z.; Kane, L. C.; Dekker, C. High-Field Electrical Transport in Single-Wall Carbon Nanotubes. *Phys. Rev. Lett.* **2000**, *84*, 2941.
- (13) Javey, A.; Guo, J.; Paulsson, M.; Wang, Q.; Mann, D.; Lundstrom, M.; Dai, H. High-Field Quasiballistic Transport in Short Carbon Nanotubes. *Phys. Rev. Lett.* **2004**, *92*, 106804.
- (14) Perebeinos, V.; Tersoff, J.; Avouris, Ph. Electron-Phonon Interaction and Transport in Semiconducting Carbon Nanotubes. *Phys. Rev. Lett.* **2005**, *94*, 086802.
- (15) Liu, K. H.; Deslippe, J.; Xiao, F. J.; Capaz, R. B.; Hong, X. P.; Aloni, S.; Zettl, A.; Wang, W. L.; Bai, X. D.; Louie, S. G.; Wang, E. G.; Wang, F. An Atlas of Carbon Nanotube Optical Transitions. *Nat. Nanotechnol.* **2012**, *7*, 325–329.
- (16) DeBorde, T.; Aspirtarte, L.; Sharf, T.; Kevek, J. W.; Minot, E. D. Determining the Chiral Index of Semiconducting Carbon Nanotubes Using Photoconductivity Resonances. *J. Phys. Chem. C* **2014**, *118*, 9946–9950.
- (17) Liu, K. H.; Hong, X. P.; Choi, S.; Jin, C. H.; Capaz, R. B.; Kim, J.; Wang, W. L.; Bai, X. D.; Luoie, S. G.; Wang, E. G.; Wang, F. Systematic Determination of Absolute Absorption Cross-Section of Individual Carbon Nanotubes. *Proc. Natl. Acad. Sci. U. S. A.* **2014**, *111*, 7564–7569.
- (18) Malapanis, A.; Perebeinos, V.; Sinha, D.; Comfort, E.; Lee, J. Quantum Efficiency and Capture Cross Section of First and Second Excitonic Transitions of Single-Walled Carbon Nanotubes Measured Through Photoconductivity. *Nano Lett.* **2013**, *13*, 3531–3538.
- (19) Qiu, X. H.; Freitag, M.; Perebeinos, V.; Avouris, P. Photoconductivity Spectra of Single-Carbon Nanotubes: Implications on the Nature of Their Excited States. *Nano Lett.* **2005**, *5*, 749–752.

- (20) Kumamoto, Y.; Yoshida, M.; Ishii, A.; Yokoyama, A.; Shimada, T.; Kato, Y. K. Spontaneous Exciton Dissociation in Carbon Nanotubes. *Phys. Rev. Lett.* **2014**, *112*, 117401.
- (21) Dukovic, G.; Wang, F.; Song, D.; Sfeir, M.; Heinz, T.; Brus, L. Structural Dependence of Excitonic Optical Transitions and Band-Gap Energies in Carbon Nanotubes. *Nano Lett.* **2005**, *5*, 2314–2318.
- (22) Pop, E.; Mann, D.; Cao, J.; Goodson, K.; Dai, H. Negative Differential Conductance and hot Phonons in Suspended Nanotube Molecular Wires. *Phys. Rev. Lett.* **2005**, *95*, 155505.
- (23) Perebeinos, V.; Rotkin, S. V.; Petrov, A. G.; Avouris, P. The Effects of Substrate Phonon Mode Scattering on Transport in Carbon Nanotubes. *Nano Lett.* **2009**, *9*, 312–316.
- (24) Wang, F.; Dukovic, G.; Brus, L. E.; Heinz, T. F. Time-Resolved Fluorescence of Carbon Nanotubes and its Implication for Radiative Lifetimes. *Phys. Rev. Lett.* **2004**, *92*, 177401.
- (25) Javey, A.; Guo, J.; Farmer, D.; Wang, Q.; Wang, D.; Gordon, R.; Lundstrom, M.; Dai, H. Carbon Nanotube Field-Effect Transistors with Integrated Ohmic Contacts and High-K Gate Dielectrics. *Nano Lett.* **2004**, *4*, 447–450.
- (26) Zhang, Z. Y.; Liang, X. L.; Wang, S.; Yao, K.; Hu, Y. F.; Zhu, Y. Z.; Chen, Q.; Zhou, W. W.; Li, Y.; Yao, Y. G.; Zhang, J.; Peng, L. M. Doping-Free Fabrication of Carbon Nanotube Based Ballistic CMOS Devices and Circuits. *Nano Lett.* **2007**, *7*, 3603–3607.
- (27) Hertel, T.; Martel, R.; Avouris, Ph. Manipulation of Individual Carbon Nanotubes and Their Interaction with Surfaces. *J. Phys. Chem. B* **1998**, *102*, 910–915.
- (28) Léonard, F.; Talin, A. Size-Dependent Effects on Electrical Contacts to Nanotubes and Nanowires. *Phys. Rev. Lett.* **2006**, *97*, 026804.
- (29) Cummings, A.; Léonard, F. Electrostatic Effects on Contacts to Carbon Nanotube Transistors. *Appl. Phys. Lett.* **2011**, *98*, 263503.
- (30) Léonard, F.; Tersoff, J. Role of Fermi-Level Pinning in Nanotube Schottky Diodes. *Phys. Rev. Lett.* **2000**, *84*, 4693.
- (31) Yaish, Y.; Park, J.; Rosenblatt, S.; Sazonova, V.; Brink, M.; McEuen, P. Electrical Nanoprobing of Semiconducting Carbon Nanotubes Using an Atomic Force Microscope. *Phys. Rev. Lett.* **2004**, *92*, 046401.
- (32) Xu, H. T.; Wang, S.; Zhang, Z. Y.; Peng, L. M. Length Scaling of Carbon Nanotube Electric and Photo Diodes down to Sub-50 nm. *Nano Lett.* **2014**, *14*, 5382–5389.
- (33) Harrah, D. M.; Swan, A. K. The role of Length and Defects on Optical Quantum Efficiency and Exciton Decay Dynamics in Single-Walled Carbon Nanotubes. *ACS Nano* **2011**, *5*, 647–655.
- (34) Graham, M. W.; Chmeliov, J.; Ma, Y.-Z.; Shinohara, H.; Green, A. A.; Hersam, M. C.; Valkunas, L.; Fleming, G. R. Exciton Dynamics in Semiconducting Carbon Nanotubes. *J. Phys. Chem. B* **2011**, *115*, 5201–5211.
- (35) Chmeliov, J.; Narkeliumas, J.; Graham, M. W.; Fleiming, G. R.; Valkunas, L. Exciton-Exciton Annihilation and Relaxation Pathways in Semiconducting Carbon Nanotubes. *Nanoscale* **2016**, *8*, 1618–1626.
- (36) Harrah, D. M.; Schneck, J. R.; Green, A. A.; Hersam, M. C.; Ziegler, L. D.; Swan, A. K. Intensity-Dependent Exciton Dynamics of (6,5) Single-Walled Carbon Nanotubes Momentum Selection Rules, Diffusion, and Nonlinear Interactions. *ACS Nano* **2011**, *5*, 9898–9906.
- (37) Wang, F.; Dukovic, G.; Knoesel, E.; Brus, L. E.; Heinz, T. Observation of Rapid Auger Recombination in Optically Excited Semiconducting Carbon Nanotubes. *Phys. Rev. B: Condens. Matter Mater. Phys.* **2004**, *70*, 241403.
- (38) Manzoni, C.; Gambetta, A.; Menna, E.; Meneghetti, M.; Lanzani, G.; Cerullo, G. Intersubband Exciton Relaxation Dynamics in Single-Walled Carbon Nanotubes. *Phys. Rev. Lett.* **2005**, *94*, 207401.
- (39) Kinder, J. M.; Mele, E. J. Nonradiative Recombination of Excitons in Carbon Nanotubes Mediated by free Charge Carriers. *Phys. Rev. B: Condens. Matter Mater. Phys.* **2008**, *78*, 155429.
- (40) Yang, L. j.; Wang, S.; Zeng, Q. S.; Zhang, Z. Y.; Pei, T.; Li, Y.; Peng, L. M. Efficient Photovoltage Multiplication in Carbon Nanotubes. *Nat. Photonics* **2011**, *5*, 672–676.
- (41) Wei, N.; Yang, L.; Xie, H. H.; Wei, F.; Wang, S.; Peng, L. M. Carbon Nanotube Light Sensors with Linear Dynamic Range of over 120 dB. *Appl. Phys. Lett.* **2014**, *105*, 073107.